JOURNAL OF SPACECRAFT AND ROCKETS
Vol. 36, No. 1, January–February 1999

Aerothermodynamic Environment for a Generic Missile

Matthew E. Zuber,* Matthew C. Towne,† Alice J. Chen,‡ John J. Bertin,§ and Robert J. Butler¶
U.S. Air Force Academy, Colorado 80840-6222

There are a variety of computer codes of varying degrees of rigor that can be used by the designers of high-speed missile systems to define the aerothermodynamic environment at flight conditions. It is assumed that the flow models and the numerical algorithms used in these codes have been validated by their developers. However, the users of such codes must exercise them against a quality database, gaining knowledge of the intricacies in the use of such codes and calibrating the range of conditions over which the code can be used to predict specific parameters that are important to the design objectives without necessarily verifying that all of the features of the flow are correctly modeled. Forces and moments, surface pressures, surface temperatures, and flow-visualization photographs have been obtained in the Tri-Sonic Wind Tunnel at the U.S. Air Force Academy at Mach 4.28. When comparing the flowfield parameters computed using state-of-the-art codes with the corresponding experimental parameters, streamwise oscillations were observed in the computed pressure distribution on the windward surface of the missile at angle of attack. These anomalous results were eliminated by modifying the grid to cluster points for capturing the bow shock wave.

Nomenclature

A	= axial force
C_A	= axial-force coefficient, $A/(q_\infty S)$
C_M	= pitching-moment coefficient referenced to the apex of the model, $M/(q_\infty S D)$
C_N	= normal-force coefficient, $N/(q_\infty S)$
D	= diameter of the cylindrical portion of the model, 1.25 in.
L	= model length, 10.00 in.
M	= pitching moment referenced to the apex of the model
N	= normal force
P	= static pressure
P_{t1}	= total pressure in the tunnel reservoir
R_n	= nose radius
$Re_{\infty,L}$	= Reynolds number based on the freestream conditions and on the model length
ReL	= Reynolds number based on the freestream conditions and on the model length in millions, i.e., $Re_{\infty,L} \times 10^{-6}$
r	= recovery factor
S	= reference area, $\pi D^2/4$
s	= wetted distance from the apex of the model
T_{recovery}	= recovery temperature; see Eq. (5)
T_{t1}	= total temperature in the tunnel reservoir
V	= velocity
x, y, z	= physical coordinates; see Fig. 3
x_{cp}	= distance from the apex of the model to the center of pressure, as measured along the model axis
α	= angle of attack
ε, η, ζ	= coordinate system for the GASPv3 computations (axial, semicircumferential, and normal)
μ	= viscosity
ρ	= density
φ	= angle measured relative to the leeward plane of symmetry

Subscripts

atm	= atmospheric pressure
eff	= effective angle of attack, the sum of the specified and the offset angles of attack; see Eq. (2)
$t1$	= conditions in the reservoir (or stilling chamber) of the Tri-Sonic Wind Tunnel
1 or ∞	= freestream conditions

Introduction

THE designers of high-speed missile systems make extensive use of computer codes to define the aerothermodynamic environment at flight conditions. Reliance on computational fluid dynamic (CFD) codes for predicting the flight environment is due in part to the inability of ground-test facilities to provide a complete match of all of the pertinent simulation parameters for the flowfields and in part to rapid advances in computer hardware and software. There are many sophisticated codes that apply the Navier–Stokes equations (in varying degrees of rigor) to the entire flowfield. Some codes are used primarily by the organization responsible for their development, e.g., the LAURA code.[1] Other codes, which have been widely distributed, are used by organizations throughout the world, e.g., the GASPv3 code.[2] The developers of such computational codes must first determine what fluid-dynamic phenomena are important to the expected applications of the code. Numerical models of suitable rigor must be developed for the important fluid-dynamic phenomena. Once the numerical models have been developed, the code developers must validate them and determine the range of conditions over which the models are valid. Bradley[3] defines the concept of code validation as follows:

> CFD code validation implies the comparison of detailed surface and flowfield parameters with the corresponding experimental values to verify the code's ability to model accurately the critical physics of the flow. Validation can occur only when the accuracy and limitations of the experimental data are known and thoroughly understood and when the accuracy and limitations of the code's numerical algorithms, grid density effects, and physical basis are equally known and understood over a range of specified parameters.

Mehta[4] states:

> Validation is defined as the process of assessing the credibility of the simulation model, within its domain of applicability, by determining whether the right simulation model is developed and by estimating the degree to which this model is an accurate representation of reality from the perspective of its intended uses.

Received Oct. 5, 1997; revision received Oct. 1, 1998; accepted for publication Nov. 9, 1998. This paper is declared a work of the U.S. Government and is not subject to copyright protection in the United States.

*Research Engineer, Department of Aeronautics. Member AIAA.
†Assistant Professor, Department of Aeronautics; currently Computational Specialist, Lockheed Martin Tactical Aircraft Systems, MZ 4263, P.O. Box 748, Ft. Worth, TX 76101. Senior Member AIAA.
‡Deputy for Operations, Department of Aeronautics. Senior Member AIAA.
§Professor of Aeronautics, Department of Aeronautics. Fellow AIAA.
¶Assistant Deputy for Operations, Department of Aeronautics. Senior Member AIAA.

Bradley[3] defines the concept of code calibration as follows:

> CFD code calibration implies the comparison of CFD code results with experimental data for realistic geometries that are similar to the ones of design interest, made in order to provide a measure of the code's ability to predict specific parameters that are important to the design objectives without necessarily verifying that all the features of the flow are correctly modeled.

Bradley has stated:

> Engineers have always been able to use less than perfect tools coupled with experiences and calibration to known physical quantities to provide design guidance. Calibration and validation should not be confused. Calibration provides an error band or correction factor to enhance the ability of a particular code to predict specific parameters that are important to the design objectives for a particular design without verifying that all other features of the flow are modeled accurately. For example, one might calibrate a code's ability to predict shock location and lift and moment on a wing without any assurances that the flowfield off the surface and the wake behind the wing are properly modeled. Or one may calibrate a code's ability to compute the gross pressure loss through a supersonic inlet-duct combination without concern for the distortion distribution at the compressor face. Although the use of calibrated CFD solutions is dangerous because of the subtle viscous interactions that are extremely sensitive to geometry and flowfield, skilled engineers can often obtain useful design information and guidance from relatively immature codes.

There are a variety of codes that employ relatively simple analytical models, empirical correlations, and two-layer flowfield models (Euler equations to model the inviscid flow coupled with a boundary-layer formulation). As noted by Martellucci[5]: "These approximate techniques are very efficient, typically requiring only seconds on small computers, and are 'robust' in the sense of almost always producing a solution." Several organizations have developed a family of design codes that provide engineering level or preliminary-design estimates of aerodynamic forces and moments acting on missiles of arbitrary shapes flying at supersonic/hypersonic speeds. These design codes include M3HAX,[6] NSWC AP95 (Ref. 7), and Missile DATCOM.[8] As discussed in Refs. 6–8, these codes are continually being modified to improve the existing models for flow phenomena and to add subroutines that can address new problems. Another code that employs approximate techniques is the ATAP code.[9]

Data that can be used to define the aerothermodynamic environment of a generic missile have been obtained in the Tri-Sonic Wind Tunnel (TWT) of the Aeronautical Research Center (ARC) at the U.S. Air Force Academy. Forces and moments, surface pressures, surface temperatures, and flow-visualization photographs have been obtained at a Mach number of 4.28 over a range of Reynolds numbers (based on the freestream conditions and model length) from 1×10^7 to 1.5×10^7. The experimentally determined parameters are compared in the present article with parameters computed using the parabolized Navier–Stokes equations in the GASPv3 code and with the aerodynamic coefficients computed using the ATAP code.[9] The objectives of the comparisons include 1) the verification of the quality of the data from the TWT and 2) the continuation of the effort to calibrate the computational tools available to the ARC/Department of Aeronautics for teaching and for research.

Experimental Program

Facility

The experimental investigation utilized the TWT, which is a blow-down facility that discharges to the atmosphere. A pair of rotary screw-type compressors generates the compressed air for the wind tunnel. From the compressors, the air is routed through a pair of drying towers and stored in six holding tanks. The dew point of the dried air is -50°F, when the tank temperature is 100°F and the tank pressure is 600 psia. As a result, the absolute humidity of the dried air is less than 2×10^{-6} lb H_2O per pound dry air. During a run, the air passes from the holding tanks, through a series of control valves, into a stilling chamber, through a convergent/divergent nozzle, and into the 1×1 ft test section. The total pressure in the stilling chamber is sensed by a transducer with a full-scale range of 300 psia with a combined nonlinearity and hysterises of $\pm 0.3\%$ full scale. The maximum total pressure in the stilling chamber, which occurs at the higher Mach numbers, is 250 psia. The total temperature in the stilling chamber is sensed by a type E (chromel/constantan) thermocouple capable of measuring -328 to 1652°F with a sensitivity of 37.7 μV/°F. The total temperature varies only slightly, being $560 \pm 20^\circ$R. Usable run times range from 20 to 420 s.

Instrumentation

The static pressures acting on the model surface were transmitted through a pressure orifice formed by stainless-steel tubing, which had an inside diameter of 0.0310 in. and was mounted flush to the model surface. The pressures then passed through approximately 10 ft of Tygon® tubing, which had an inside diameter of 0.0313 in. and an outside diameter of 0.0938 in., to a Scani-valve® that housed the pressure transducer. For the present tests, a Kulite® differential-pressure transducer with a full-scale range of 15 psid (differential) and a combined nonlinearity and hysterises of $\pm 0.5\%$ full scale was used to measure the gauge pressure relative to the static pressure in the room. The reference pressure, i.e., the static pressure in the room, was measured by a Heise® digital pressure indicator with a full-scale range of 17.19 psia. Including the effects of sensitivity, hysterises, nonlinearity, and repeatability, the atmospheric pressure measurement had an uncertainty of $\pm 0.035\%$ of the full-scale measurement at 70°F. Because of the long length of Tygon tubing connecting the pressure orifice in the model to the Scani-valve/transducer, all pressure measurements were time-averaged, steady-state values. Once the flow was established, there was a 3000-ms delay before the first pin of the Scani-valve was recorded. There was a 200-ms delay between each of the subsequent steps.

A six-component force and moment balance was used to sense the forces and the moments acting on the models. The balance provided measurements that could be used to determine the axial force, the side force, the normal force, the pitching moment, the rolling moment, and the yawing moment. Two pressure orifices were located on the model support system, i.e., the sting, just downstream of the model base to provide a measure of the base pressure. The locations of these two orifices are diametrically opposed (so that they are located ± 90 deg, from the leeward plane of symmetry). The capability and the accuracy of the individual components of the six-component balance were N1: 100 lbf $\pm$ 0.25% full scale, N2: 100 lbf $\pm$ 0.25% full scale, Y1: 50 lbf $\pm$ 0.25% full scale, Y2: 50 lbf $\pm$ 0.25% full scale, axial: 25 lbf $\pm$ 0.25% full scale, and rolling moment: 60 in lbf $\pm$ 0.25% full scale. Therefore, the uncertainty of a given axial-force measurement was ± 0.0625 lbf. Because typical measured values of the axial force were in the range 5–10 lbf, the corresponding uncertainties (given as a percent of that measured value) are $+1.25$ to 0.63%, respectively. When the model was at an angle of attack of ± 10 deg, typical maximum values of the normal force were 28 lbf. Thus, the corresponding uncertainty is 0.2% of this measured value for the normal force.

Thermochromic liquid crystals (TLCs), i.e., temperature-sensitive liquid crystals, were used in the present experimental program to obtain qualitative and quantitative information about the heat-transfer distributions. By using a TLC with a specific color-play band over which the liquid crystal changed color, one could determine when the model surface passed through a certain temperature range, as the model cooled during the run, starting from room temperature. Specifically, the TLC used in the present tests was a Hallcrest® BM/R12C1W/C17-10 TLC with a 0.9°F bandwidth and the color play starting at 55.3°F and ending at 54.4°F. By observing the color patterns of the TLC coating on the model surface, one can identify regions of locally high heat transfer, locate the onset of boundary-layer transition, and identify regions where the flow has separated from the model. By recording the time required for the surface temperature at a certain location to pass through the color-play temperature range, one can determine the magnitude of the local heat transfer. Several studies have been conducted to develop techniques through which one can use TLCs to quantify the aerothermodynamic environment of models exposed to high-speed

flows.[10,11] The thermal properties of the model, i.e., the thermal conductivity, the density, and the specific heat, are critical to the quantitative determination of the local heat transfer. The model for the present tests was made of Ertalyte®.

Test Conditions

The freestream Mach number in the test section was 4.28 ± 0.04. This is the average value determined from a facility calibration program in which an 11-probe pitot rake was rotated in 30-deg increments. These pitot-pressure measurements were used to generate Mach number contours for three planes in the test section: one at the upstream end, a second in the middle, and the third at the downstream end of the test section. The nominal value of the test-section Mach number has been verified in repeated investigations of the flow quality of the TWT. Force-and-moment data were obtained at three nominal values of the total pressure in the tunnel reservoir, P_{t1}; specifically, $P_{t1} = 150$, 200, and 225 psia. Pressure measurements were obtained at a single (nominal) value of $P_{t1} = 200$ psia. There was a single (nominal) total temperature for all of the runs, $T_{t1} = 560°\text{R}$.

The perfect-gas relations were used to calculate the freestream conditions, assuming that the flow accelerated isentropically from the nominal stagnation conditions to the Mach 4.28 freestream. Sutherland's equation[12] was used to calculate the freestream viscosity. However, as noted in Ref. 12, "one would expect that the actual viscosity is 3 percent to 5 percent greater than Sutherland's value" at the temperatures characteristic of the freestream flow in a supersonic/hypersonic wind tunnel. When $P_{t1} = 200$ psia, the freestream unit Reynolds number is

$$Re_\infty/\text{ft} = \rho_1 V_1/\mu_1 = 16.3 \times 10^6/\text{ft}$$

The freestream Reynolds number based on the length of the model, $Re_{\infty L}$, is 13.6×10^6.

In this paper, we will sometimes use the shorthand notation ReL for the Reynolds number based on the freestream conditions and the model length in millions:

$$Re_{\infty L} = \rho_1 V_1 L/\mu_1 = ReL \times 10^6 \tag{1}$$

Because the freestream Mach number and the total temperature were essentially the same for all runs, the Reynolds number and the dynamic pressure were directly proportional to the total pressure. Thus, for a nominal value of $P_{t1} = 150$ psia, Reynolds number based on the freestream conditions was approximately 9.95×10^6; for a nominal value of $P_{t1} = 200$ psia, it was approximately 13.6×10^6; and for a nominal value of $P_{t1} = 225$ psia, it was approximately 15.2×10^6 .

Model

A two-view, dimensioned sketch of a generic missile wind-tunnel configuration is presented in Fig. 1. The overall length of the wind-tunnel configuration, L is 10.00 in. Thus, the length-to-diameter ratio (L/D), where D is the diameter of the cylindrical portion of the missile, is 8.00. There were actually several wind-tunnel models built for these wind-tunnel tests. The force-and-moment model was constructed in two parts: a forebody made of aluminum and an afterbody of brass for the fin section. Once the force-and-moment phase of the test program had been completed, the model was modified by adding 15 static pressure orifices to provide information about the surface pressure distribution. All of the heat-transfer models were made from one piece of Ertalyte.

Some dimensions of the Ertalyte heat-transfer models were different than those of the metal pressure models, which are shown in Fig. 1. The nose radius of the pressure model was 0.064 in., whereas it was 0.056 in. for the heat-transfer models. The conical half-angles were 9.4 and 9.0 deg for the pressure and for the heat-transfer models, respectively. The cylindrical section started at 3.468 in. from the nose for the pressure model and at 3.691 in. from the nose for the heat-transfer models. For all models, the diameter of the cylindrical portion of the model was 1.250 in., and the axial distance from the apex to the leading edge of the fins was 8.125 in. As shown in Fig. 1, the rectangular fins had a root chord of 1.875 in., with a tip-to-tip dimension (or span) of 3.75 in., and an airfoil half-angle (or deflection angle) for the leading and trailing edges of 9.7 deg.

Data were obtained either with two fins in the vertical plane, as shown in Fig. 1, which is designated the + configuration or with the model rotated 45 deg, the × configuration or cruciform fin configuration. Each time the configuration was changed or the model was rotated on the sting so that the orientation went from the + configuration to the × configuration or vice versa, the model had to be refastened to the sting. Although care was always taken in positioning the model, the model could not be perfectly aligned with the tunnel centerline. The misalignment angle in the pitch plane (or α_{off}) was measured before and after almost every run. The offset angle of attack was added to the specified angle of attack to obtain the effective angle of attack for a given run:

$$\alpha_{\text{eff}} = \alpha_{\text{spec}} + \alpha_{\text{off}} \tag{2}$$

A correction for the sting deflection due to wind-on aerodynamic loads is not included in Eq. (2). Wind-on corrections for the sting deflection were not measured in the present program. However, wind-on angle-of-attack measurements taken from schlieren photographs on a similar model during a previous program showed no consistent or significant correction.

Comments Regarding Uncertainty and Repeatability

The experimental pressures are usually presented as the pressure measurement for a particular orifice, P, divided by the calculated value of the freestream static pressure P_1, yielding the dimensionless pressure parameter P/P_1. A typical value of the pressure measured at the orifice located on the conical surface at zero angle of attack is 1.643 psia. Let us assume that the freestream Mach number is 4.28 and that the stilling chamber pressure P_{t1} is 200.0 psia. The corresponding value of P_1 is 0.9130 psia, and the nominal value for the dimensionless parameter for the pressure measurement is 1.80.

The measured pressure is determined as the sum of the differential pressure sensed by the Kulite pressure transducer located in the Scani-valve and the atmospheric pressure given by the Heise digital pressure indicator:

$$P = \Delta P_{\text{Kulite}} + P_{\text{atm}}$$

For the present example, the differential pressure sensed by the Kulite transducer is -9.557 ± 0.075 psig and the atmospheric pressure is 11.200 ± 0.006 psia. Combining the extremes of the uncertainties, the measured pressure could be as high as 1.724 psia or as low as 1.562 psia. Thus, the measured pressure at this orifice (which is in a region of the model unaffected by viscous/inviscid interactions) is 1.643 psia $+4.9\%/-5.0\%$.

The freestream static pressure P_1 is calculated using

$$P_1 = (P_1/P_{t1})P_{t1} = \left(\left\{1 + [(\gamma - 1)/2]M_1^2\right\}^{-[\gamma/(\gamma-1)]}\right)P_{t1} \tag{3}$$

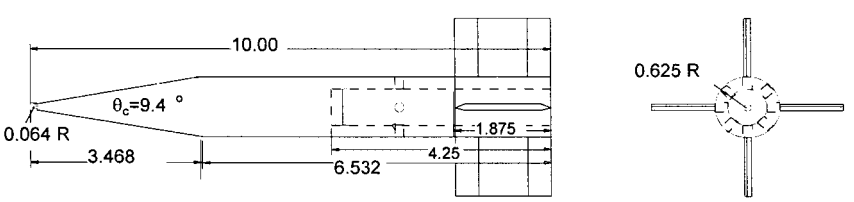

Fig. 1 Generic missile model. Dimensions: inches; $R_n/D = 0.05$ and $L/D = 8.0$.

Thus, there are two sources of uncertainty: the uncertainty in the pressure ratio because the freestream Mach number can be as low as 4.24 or as high as 4.32 and the uncertainty in the stagnation pressure measurement itself. Combining the extremes of the uncertainties, the calculated value of P_1 could be as high as 0.9655 psia or as low as 0.8635 psia. Thus, the reference pressure is 0.9130 psia $+5.75\%/-5.42\%$. Combining these results, for this hypothetical case, P/P_1 could be as low as 1.562 or as high as 1.724, which represents an uncertainty band of $+11.1\%/-10.1\%$ about the nominal value of 1.80. However, if one neglects the uncertainty in the freestream pressure due to the uncertainty in the freestream Mach number, the uncertainty in P/P_1 is approximately $\pm 6\%$.

Numerical Analysis

Using the shock-capturing GASPv3 code,[2] the steady-state, axisymmetric flowfield for a finless missile (which otherwise has the dimensions of the configuration shown in Fig. 1) was computed for 0-, 10-, and 20-deg angles of attack. The nose region flowfield was calculated using the thin-layer Navier–Stokes (TLNS) equations, whereas the parabolized Navier–Stokes (PNS) equations were used to solve the flowfield aft of the nose region. GASPv3 offers numerous solution options to the user. The inviscid flux vectors were computed to second-order accuracy using van Leer's flux-vector splitting technique combined with the van Albada limiter to maintain stability and eliminate numerical oscillations in regions containing large gradients. The two-factor approximate factorization time-integration scheme was used to solve both the TLNS equations and the PNS equations. Solutions for the nose region were considered converged when the residual had decreased by two orders of magnitude. For the region where the PNS equations were used, solutions were considered converged when the residual had decreased by three orders of magnitude. Freestream flow conditions were specified at the inflow and at the far-field boundaries upstream of the bow shock wave. A second-order extrapolation boundary condition was specified for the downstream, out-flow boundaries. Boundary conditions at the surface of the vehicle included a velocity boundary condition and a thermal boundary condition. The velocity boundary condition was the commonly used requirement that there is no slip at the wall. Because the surface temperature changes during a run, flowfield computations were made for a range of realistic thermal boundary conditions. At the start of the run, the model is at room temperature, which is approximately 540°R. The model cools during the run, approaching the recovery temperature for long-duration runs. Therefore, flowfield computations were made for two assumed thermal boundary conditions at the wall: 1) The wall temperature is uniform at approximately 540°R. 2) There is no heat transferred from the air, i.e., the adiabatic wall assumption. Observations of the liquid-crystal patterns recorded during the present program indicated that boundary-layer transition occurred roughly $0.1L$ from the nose of the model (for low angles of attack). Thus, to cover the range of possible boundary-layer characteristics, computations were made assuming both that the boundary layer is fully turbulent starting at $x = 0.1L$ and that the boundary layer remains laminar for the entire length of the model.

The ATAP empirical aerodynamic routine integrates pressure and viscous force components over the surface of multiconic missiles with fins to calculate aerodynamic coefficients. The empirical correlations for pressure and shear include the effects of Mach number, of Reynolds number, and of boundary-layer transition for continuum flows, and use Knudsen-number-based correlations to bridge to free-molecular flows. In the ATAP code, continuum-flow pressure relationships are developed separately for stagnation-region, compression, expansion, and base flows. Different relationships are used for subsonic, supersonic, and hypersonic flow and are further subdivided by the orientation of the body surface with respect to the freestream velocity vector. For the range of Mach number, of Reynolds number, and of angle of attack relevant to the present tests in the TWT, only the supersonic, continuum-flow relations are of interest.

The pressure at the stagnation point on the missile is determined by iteratively solving the Rankine–Hugoniot equations across the bow shock wave and then isentropically decelerating the flow to zero velocity. The static pressures near the stagnation point of a spherical nose cap are calculated using a modified-Newtonian-flow model. A combination of tangent-cone and of hypersonic-similarity methods is used to compute the pressure coefficient for supersonic, conical-surface compression flows on the missile body. The tangent-cone method of Gentry et al.[13] is used for Mach numbers in the range of 1.5–3.5, but does not include bluntness effects. The method of Hecht and Nestler[14] for hypersonic flows, which includes the effect of nose bluntness on the pressure distribution, has been extended to cover Mach numbers from the original hypersonic regime down to 5. The Hecht and Nestler method is bridged with the tangent-cone method between Mach 3.5 and 5. Fin side-facet pressures are computed using the correlation of Hankey[15] for compression flows and using the Prandtl–Meyer function for expansion flows. Fin/body interaction effects are modeled with the correlation of Graham and McDowell.[16] Viscous shear is modeled using simple correlations from the U.S. Air Force DATCOM code.[17]

Supersonic conical-surface expansion flows are computed assuming the flow accelerates isentropically from the freestream conditions to the local flow-inclination angle using the Prandtl–Meyer function. For base flows or for very strong expansion flows, the base pressure is tabulated as a function of the Mach number.

Discussion of Results

As noted by Bertin et al.,[18] the four types of data that can be used for code-validation/code-calibration exercises are 1) global measurements, such as the overall force and moment coefficients; 2) measurements at the surface of the vehicle or of the model, such as the static pressure at the surface or the temperatures of the surface; 3) flow-visualization techniques; and 4) measurements at points within the shock layer. Only data of the first three types will be presented in this paper.

Global Measurements

The experimental values of the global aerodynamic parameters: C_N, C_M, x_{cp}/L, and C_A are presented for the + configuration as functions of the effective angle of attack in Fig. 2. The force-and-moment data were obtained for a Mach 4.28 stream of air for freestream Reynolds numbers based on model length of 15.2×10^6, 13.6×10^6, and 9.94×10^6. To obtain data over an angle-of-attack range from -10 to $+20$ deg, two different model-support stings were used. When the straight sting was used to support the model, data could be obtained in the angle-of-attack range from -10 to $+10$ deg. When the model was supported by the bent sting, data could be obtained in the angle-of-attack range 0 to $+20$ deg. The experimentally determined values of the global aerodynamic parameters are compared with the corresponding values computed using the ATAP code[9] over a range of angles of attack from -10 to $+20$ deg.

The experimental values of the normal-force coefficient are independent of the freestream Reynolds number and of which sting was used (Fig. 2a). The normal-force coefficients are a linear function of the angle of attack from -6 to $+6$ deg. The agreement between the experimental values of C_N and the values computed using the ATAP code is considered reasonable, with the differences increasing as the angle of attack increases.

The experimental values of the pitching-moment coefficient, as referenced to the apex of the model, are presented in Fig. 2b. Again, the data are independent of the freestream Reynolds number and of which sting was used. The experimentally determined pitching-moment coefficients are in good agreement with the values computed using the ATAP code over the entire range of angles of attack tested.

Because the pitching moment is referenced to the apex of the model, the center of pressure was determined from the measurements using the approximation

$$x_{cp} = M/N \tag{4}$$

The experimental and the ATAP-computed values of the nondimensionalized center-of-pressure location (x_{cp}/L) are in reasonable agreement (Fig. 2c).

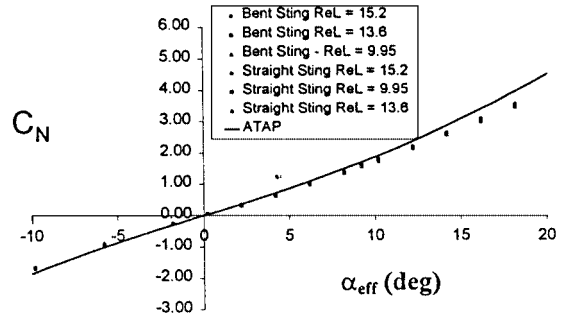

a) Normal force coefficient

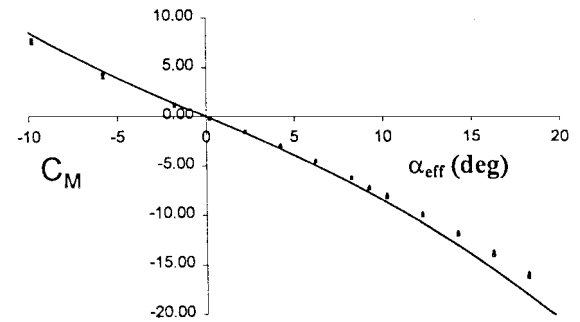

b) Pitching moment coefficient

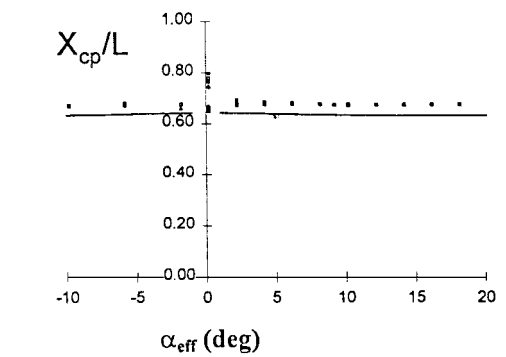

c) Center of pressure divided by the length

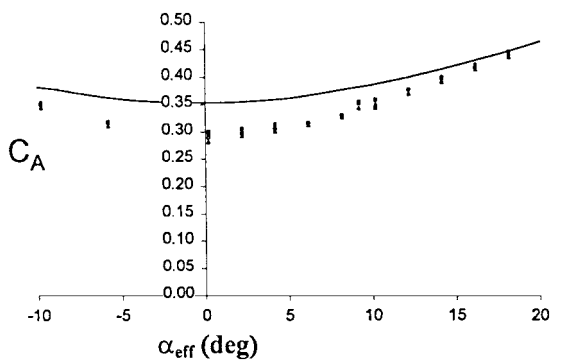

d) Axial force coefficient

Fig. 2 Experimentally determined aerodynamic parameters for a generic missile in the + configuration as a function of the effective angle of attack in a Mach 4.28 airstream as compared with ATAP computations.

The axial-force coefficient is presented as a function of the effective angle of attack in Fig. 2d. For angles of attack less than 18 deg, the experimental values of the axial-force coefficient are independent of the Reynolds number. For angles of attack greater than 18 deg, the axial-force-coefficient measurements exhibit a slight Reynolds number dependence. However, the axial-force coefficients for other configurations tested in the present program did not always exhibit a similar Reynolds number dependence. Thus, the slight Reynolds number dependence observed at the high angle-of-attack data presented in Fig. 2d is for limited, specific data and is not a general conclusion.

At relatively low angles of attack, the experimentally determined axial force coefficients are approximately 80% of the ATAP-computed values. The difference is significantly greater than the approximately 5% uncertainty based on the combination of the uncertainty in the measured value of the axial force and in the computed value of the dynamic pressure. Referring to Fig. 2d, the experimentally determined axial-force coefficients increase more rapidly with angle of attack than do the coefficients computed using the ATAP code. There are several possible reasons for these differences. The curved bow-shock wave can significantly affect the pressure distribution over the conical surface. It is difficult to model the viscous/inviscid interaction between the boundary layer approaching the tail surfaces and the fin-induced shock-wave system. This interaction is complicated by the three dimensionality of the approach flow, which includes separated flow at the higher angles of attack. For angles of attack exceeding 12 deg, the bow shock wave intersects the fin-induced shock-wave system producing a complex shock/shock interaction, further complicating the modeling challenges. Nevertheless, the agreement between the experimentally determined axial-force coefficients and those computed using the ATAP code is considered reasonable.

Surface Measurements

In addition to comparing experimentally determined values of global parameters, e.g., the force and the moment coefficients, with the corresponding values computed using the ATAP code, the experimentally determined values of flow parameters at the surface of the model were compared with the corresponding values computed using the GASPv3 code. For the computation of the axisymmetric flowfield of the missile body at zero angle of attack, a grid containing $121 \times 81 \times 65$ nodes in the ε, η, and ζ coordinates, respectively, designated the original grid in Fig. 3a, was created with a grid-generation code. The far-field boundaries were placed far enough from the vehicle to capture the attached shock wave emanating from the nose of the missile. Points were clustered near the surface of the model, so that the distance to the first grid point off the surface is nominally $0.00036L$. As can be seen in the grid for the yz plane presented in Fig. 3a, clustering also was used in the circumferential direction to provide greater detail of the flowfield near the plane of symmetry on the leeward side of the model.

The streamwise pressure distribution for zero angle of attack is presented in Fig. 4. The experimental pressures for the conical surface of the model, i.e., $s < 0.3$ ft, exhibit an oscillatory dependence on s. The reader should note that the measurements used to develop the experimental-pressure distribution presented in Fig. 4 came from orifices on the conical surface that were alternately located in the $\varphi = 0$ deg and the $\varphi = 180$ deg planes. The existence of an offset angle of attack, which already has been discussed, caused the effective angle of attack to be either 0.1 or 0.2 deg for these data. That the model is actually at a slight angle of attack is believed to contribute to the apparent oscillatory nature of the measured pressures because consecutive measurements come from opposite sides of the conical surface. Nevertheless, the experimentally determined pressures are in reasonable agreement with the computed values for zero angle of attack. Included for comparison in Fig. 4 is the theoretical value of the pressure on a sharp cone having a conical half-angle of 10 deg in a Mach 4.28 airstream, as calculated using the charts of Ref. 19. The agreement between the theoretical value of the sharp-cone pressure, as calculated using the charts of NACA Report 1135 (Ref. 19), and the values for the pressure at the aft end of the conical frustum, as computed using GASPv3, is considered to be very good considering the differences between the actual flowfield and the flowfield for a sharp cone, which contains an attached, straight bow shock wave and which is the flow model for the Ref. 19 value.

The flowfield for an angle of attack of 20 deg was computed using the grid presented in Fig. 3a, i.e., using the original grid. The pressures, thus computed, are designated "laminar boundary layer, grid of Fig. 3a" in Fig. 5. The pressures computed for the windward plane of symmetry exhibit an oscillatory variation in the streamwise direction beginning near the end of the conical frustum and continuing

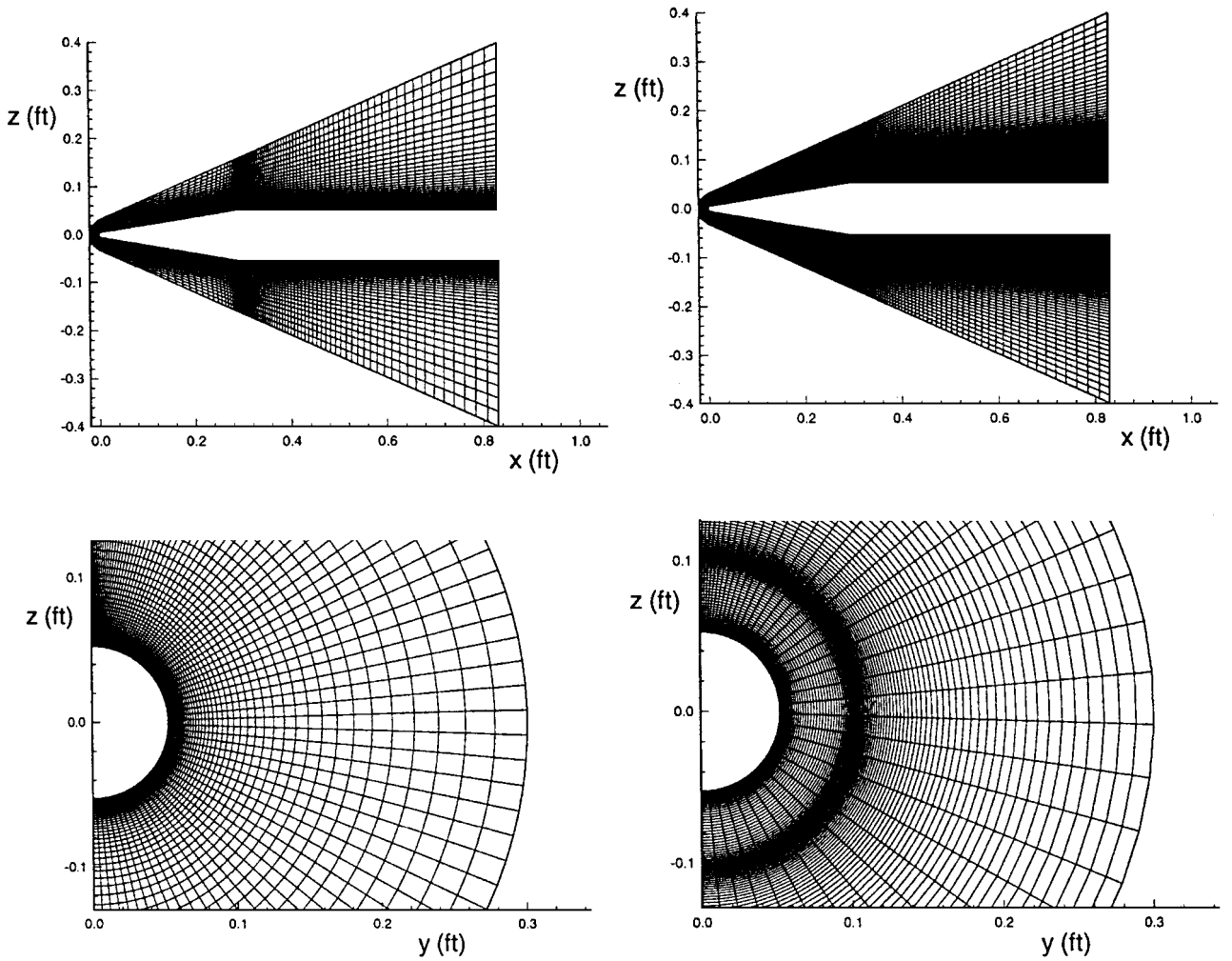

a) Original grid

b) Modified grid, clustered for capturing the bow shock wave

Fig. 3 Comparison of the grids used in the GASPv3 pressure computations.

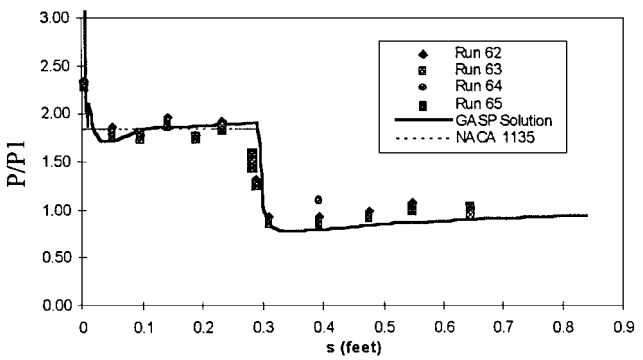

Fig. 4 Comparison of the measured surface pressures with those computed using the GASPv3 code and with the Ref. 19 value for $\alpha = 0$ deg and $ReL = 13.6$.

onto the cylindrical section. Although the pressure measurements from this region did not exhibit an oscillatory behavior in the streamwise direction, there were too few orifices to make a definitive conclusion regarding the existence of oscillations, based on the data. However, a detailed examination of the computed flowfield parameters revealed a series of expansion waves and of compression waves reflecting across the shock layer, which is consistent with the computed pressure oscillations. Furthermore, the streamwise pressure distributions computed with the number of grid points doubled and quadrupled (but maintaining the grid clustering scheme shown in Fig. 3a) exhibited oscillations similar to those presented in Fig. 5.

Because the measured pressures did not exhibit the oscillations evident in the computations, the authors of the present article discussed the anomaly with others. W. L. Oberkampf of the Sandia National Laboratories and F. G. Moore of the Naval Surface Weapons Center suggested that these pressure variations were probably anomalies associated with the computational algorithm. Green et al.[20] reported benchmark flowfield computations by three different groups, noting that total-enthalpy fields produced by two shock-capturing methods contained a small amount of numerical noise, whereas shock-fit results exhibited no oscillations. The number of grid points in the normal direction for one of the shock-capturing techniques was doubled as part of a grid-sensitivity exercise. Green et al.[20] reported that "the level of grid sensitivity is believed to be small enough that grid resolution cannot be used to explain either the examples of agreement or disagreement between the results of the three groups."

Oberkampf suggested that clustering points in the vicinity of the bow shock wave would improve the shock-capturing resolution and would, therefore, eliminate the anomalous pressure oscillations. Thus, a new grid (designated "modified grid, clustered for capturing the bow shock wave" in Fig. 3b) was developed with $121 \times 41 \times 101$ points in the ε, η, and ζ coordinates, respectively. As shown in Fig. 3b, the additional 36 points in the ζ coordinate were clustered to correspond to the expected windward, midcone location of the bow shock wave. Referring to the aft view of the modified grid, the ζ coordinate for the clustering was the same around the vehicle, i.e., was independent of the η coordinate. Despite the relatively crude nature of the clustering strategy, the pressure distributions presented in Fig. 5 did not exhibit streamwise variations (see the computed

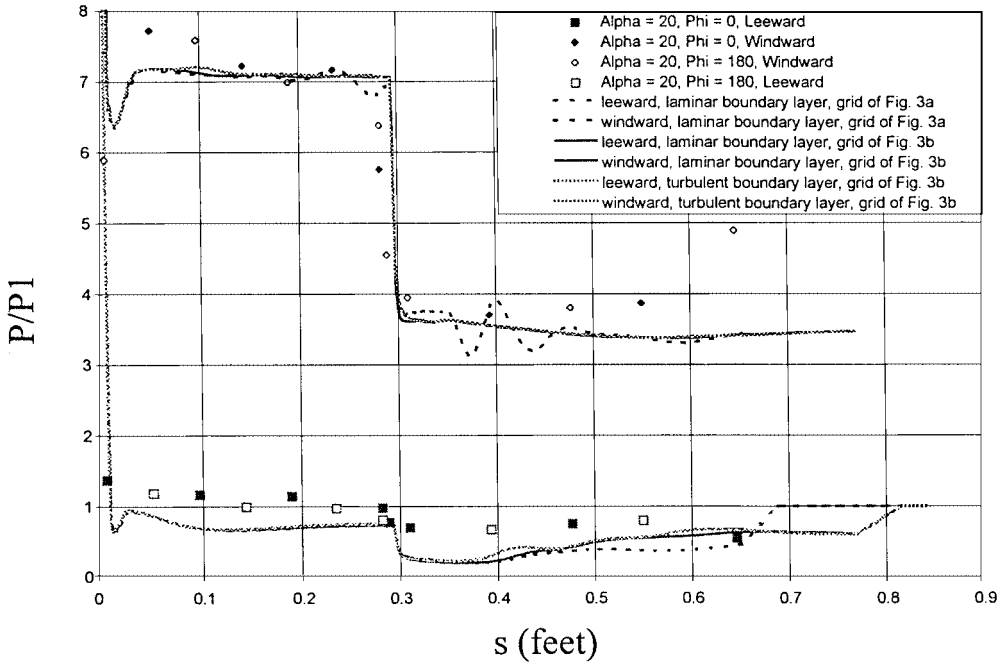

Fig. 5 Comparison of the measured surface-pressure distributions with those computed using GASPv3 illustrating the effect of grid and of the boundary-layer character for $\alpha = 20$ deg.

pressure distribution: "laminar boundary layer, grid of Fig. 3b"). That the modified clustering strategy improved the resolution of the captured shock and eliminated the expansion waves and the compression waves reflecting across the shock layer is clearly evident in the iso-Mach-number contours presented in Fig. 6. For computations made with the original grid (Fig. 6a), the captured shock wave is a braided structure and a left-running expansion fan can be seen impinging on the surface of the cylinder. For the computations made with the modified grid (Fig. 6b), the shock wave is much thinner and is captured in relatively few grid points. A right-running expansion fan is seen, originating at the cone/cylinder interface, with the flow downstream of the corner being uniform.

Because the liquid crystal data indicated that boundary-layer transition occurred at an x/L of approximately 0.1, the flowfield was computed with the boundary layer assumed to be turbulent downstream of $x = 0.1L$. The pressure distributions computed for a turbulent boundary layer are essentially the same as those computed for the laminar boundary layer using the same, modified grid (Fig. 3b).

A schlieren photograph with the model at an angle of attack of 20 deg is presented in Fig. 7a. Iso-Mach-number contours computed for the same angle of attack (and for the grid of Fig. 3b) are presented in Fig. 7b. The computed shock wave overlays perfectly onto the trace of the shock wave in the schlieren photograph. This agreement provides additional evidence that the flowfield computed with the modified grid is a reasonable approximation of the actual flowfield.

Flow Visualization

Coating the model with TLCs provided a global, visual picture of the surface temperature as a function of time. As noted earlier, the color play for the TLCs used in the present tests had a bandwidth of 0.9°F, starting at 55.3°F and ending at 54.4°F. The recovery temperature was calculated using the relation[12]

$$T_{\text{recovery}} = \left(r + \frac{1 - r}{\left\{ 1 + [(\gamma - 1)/2] M_{\text{edge}}^2 \right\}} \right) \tag{5}$$

If one assumes that the boundary layer is laminar, the recovery temperature is nominally 1.0°F, whereas it is 26.1°F, if the boundary layer is assumed to be turbulent. At the start of a run, the model is at room temperature, which is approximately 75°F. Thus, the surface temperature decreases during a run, approaching the recovery

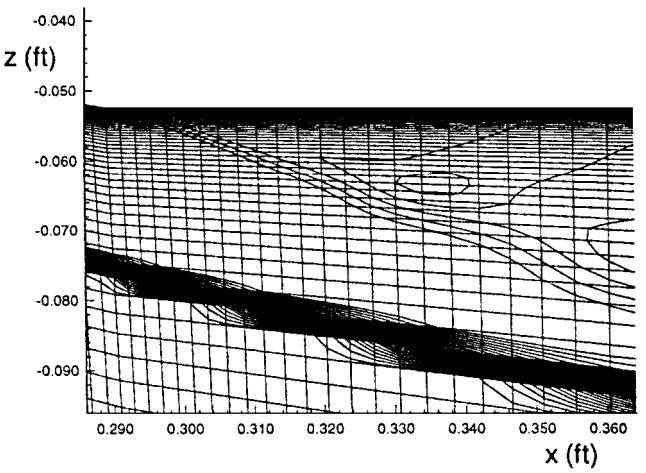

a) Computations for the original grid

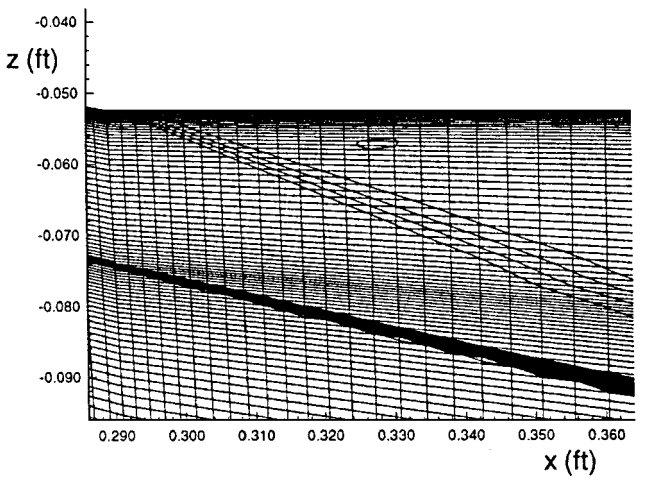

b) Computations for the modified grid, clustered for capturing the bow shock wave

Fig. 6 Comparison of the iso-Mach-number contours for GASPv3 computed flowfields for $\alpha = 20$ deg.

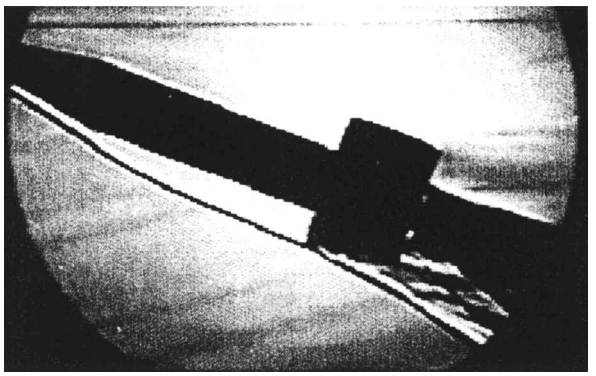

a) Schlieren photograph

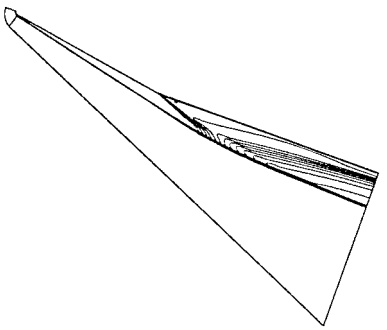

b) Iso-Mach contours as computed using GASPv3

Fig. 7 Comparison of the windward flowfields for the model at α = 20 deg.

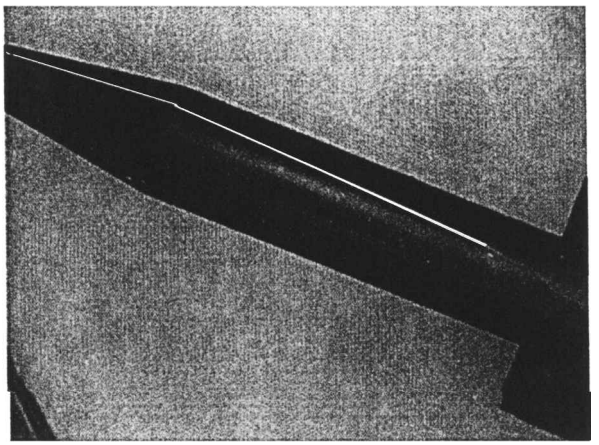

a) Separation line highlighted in TLC pattern

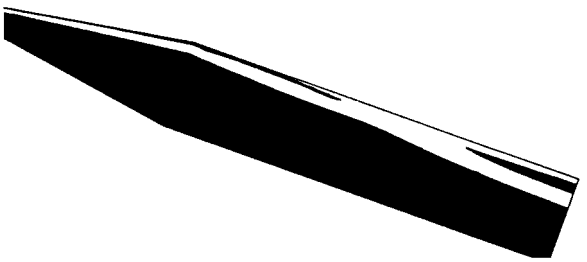

b) GASPv3 separation region is light gray scaled, whereas the attached flow is black

Fig. 8 Comparison of the separation regions for a generic missile in a Mach 4.28 airstream for α = 20 deg.

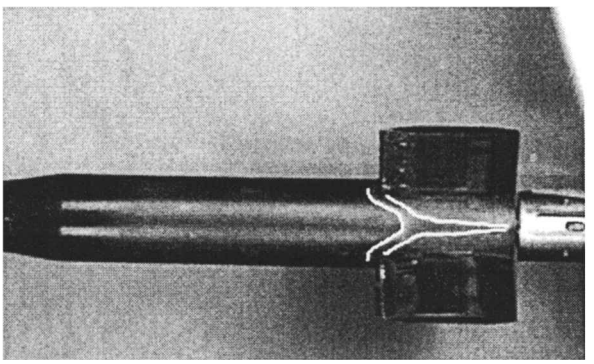

Fig. 9 TLC pattern in the vicinity of the fins of the × configuration missile in a Mach 4.28 airstream for α = 0 deg.

temperature over time. In regions where the local heat-transfer coefficient is relatively high, the model cools rapidly, quickly passing through the temperature range associated with the color play. Once the surface temperature falls below 54.4°F, the TLC coating becomes translucent, exposing the black-painted surface of the model. In regions where the local heat transfer coefficient is very low, such as would be the case in a separated-flow region, the surface temperature never reaches the color play range and the TLC coating remains blue. Thus, if the model is exposed to the airstream for a relatively long period of time, e.g., at least 30 s, the TLC coating will either be blue or translucent (black). The interface between the two colors will mark the free-vortex separation line.

The free-vortex separation line, thus determined, for the model at an angle of attack of 20 deg is highlighted in Fig. 8a. The TLC pattern has been converted from the original color TIFF file to a black-and-white TIFF file. The highlighting is necessary because the color-band difference is hard to distinguish in the black-and-white format used in the present paper. The free-vortex separation line based on the flowfield computed for an angle of attack of 20 deg is presented in Fig. 8b. To define the crossflow separation location at a given x location based on the computed flowfield, the numerical solutions were examined to determine the φ coordinate at which the circumferential velocity component at the first grid point off the surface changes sign. There was no apparent effect of Reynolds number on the separation patterns observed over the range of flow conditions covered in the present test program.

The TLC pattern presented in Fig. 9 for the missile at zero angle of attack in the × configuration or cruciform fin configuration provides significant information for the interaction flowfield in the vicinity of the fins. The fin-leading-edge bow shock wave created as the locally supersonic flow approaches the fin leading edge interacts with the approach boundary layer. The shock-induced pressure rise propagates upstream through the subsonic portion of the boundary layer, creating a λ-like shock structure in the plane of the fin. The viscous/inviscid interaction causes the flow to separate, as can be seen in the TLC pattern presented in Fig. 9. This is consistent with the flowfield presented by Nishio.[21] The interactions from the individual fins coalesce, producing a Y-shaped pattern that appears on the surface of the missile between the fins.

Concluding Remarks

Based on the data obtained over the range of conditions covered in the present program and on the comparisons of these data with parameters computed using the ATAP code and using the GASPv3 code, the following conclusions are made:

1) The experimentally determined values of C_N, C_M, and x_{cp}/L were independent of the Reynolds number and of which sting was used to support the model in the wind tunnel. The engineering models used in the ATAP code provided suitable estimates of C_N, C_M, and x_{cp}/L.

2) There were significant differences between the experimentally determined values of C_A and those computed using the ATAP code. The complex nature of the viscous/inviscid interactions involving the bow shock wave, the imbedded shock waves generated when the three-dimensional (sometimes separated) flow encounters the tail surfaces, and the base region flow contribute to these differences. Considering the approximations used in the ATAP flow models, the differences between the experimental and the computed values of the axial force coefficients are deemed acceptable.

3) It is assumed that the validation of the models used in developing these codes is the responsibility of the code developer. However, in comparing the computed results to the experimental values, streamwise oscillations were observed in the computed pressure distribution on the windward surface of the missile at angle of attack. Detailed examination of the computed parameters revealed expansion waves and compression waves reflecting across the shock layer, consistent with the pressure distribution. However, discussions with experts on such flowfields and further computations revealed that the oscillating pressure was an anomaly, associated with the use of the shock-capturing technique. Simply doubling the number of grid points in the ζ direction did not significantly change the computed pressure distribution. The anomalous results were eliminated by modifying the grid to cluster points for capturing the bow shock wave. As codes proliferate, more and more people who have had nothing to do with the development of the code will be using the code. It is important that the codes are exercised for a wide variety of applications and the results documented, so that the user community can understand the possible sources of anomalies and their effect on the computed flowfields.

Acknowledgments

The authors appreciate the financial support provided by the Air Force Research Laboratory/Armament Directorate/Munitions Seeker and Evaluation Branch (AFRL/FMGG) at the Eglin Air Force Base through Project Order QFY76219725005. Hubert G. Schneider and Tony Thompson of AFRL/FMGG served as Technical Officers for the effort. As one of the developers of the ATAP code, Jim Trolier of Science Applications International Corporation also supported the authors of this paper. The authors would like to thank the following people for their contributions to this effort: James E. Mayhew for computing the thermodynamic properties associated with the tunnel flow and both Larry Lamblin, the tunnel technician, and Bobby Hatfield, the model craftsman, whose dedication and competence were critical to the successful execution of the test program. Also, discussions with W. L. Oberkampf of Sandia National Laboratories and F. G. Moore of the Naval Surface Weapons Center are gratefully acknowledged.

References

[1]Gnoffo, P. A., Weilmuenster, K. J., and Hamilton, H. H., II, "Computational Aerothermodynamic Design Issues for Hypersonic Vehicles," AIAA Paper 97-2473, June 1997.

[2]"General Aerodynamic Simulation Program, Version 3 (GASPv3)," User's Manual, Aerosoft, Inc., Blacksburg, VA, May 1996.

[3]Bradley, R. G., "CFD Validation Philosophy," Paper 1, *AGARD Symposium on Validation of Computational Fluid Dynamics* (Lisbon, Portugal), CP-437, Vol. 1, AGARD, 1989 (Paper 1).

[4]Mehta, U. B., "Guide to Credible Computer Solutions of Fluid Flows," *Journal of Propulsion and Power*, Vol. 12, No. 5, 1996, pp. 940–948.

[5]Martellucci, A., "The Challenging Process of Validating CFD Codes," AIAA Paper 90-1402, June 1990.

[6]Dellinius, M. F. E., Lesieutre, D. J., Hegedus, M. C., Perkins, S. C., Jr., Love, J. F., and Lesieutre, T. O., "Engineering, Intermediate, and High Level Aerodynamic Prediction Methods and Applications," AIAA Paper 97-2278, June 1997.

[7]Moore, F. G., "Current Status and Future Plans of the Aeroprediction Code," AIAA Paper 97-2279, June 1997.

[8]Blake, W. B., "Missile DATCOM: 1997 Status and Future Plans," AIAA Paper 97-2280, June 1997.

[9]Trolier, J. W., Dougherty, C. M., Tincher, D. J., and Hall, D. W., "Wright Laboratory—Aerothermal Target Analysis Program (WL-ATAP Version 1.4—September 1997), Volume 2: Engineering Documentation," Science Applications International Corp., Wayne, PA, Sept. 1997.

[10]Jones, T. V., Ireland, P. T., Wang, Z., and Jones, T. V., "Liquid Crystal Techniques," International Symposium on Heat Transfer in Turbomachinery, Keynote Paper, Athens, Greece, Aug. 1992.

[11]Babinski, H., and Edwards, J. A., "Automatic Liquid Crystal Thermography for Transient Heat Transfer Measurements in Hypersonic Flow," *Experiments in Fluids*, Vol. 21, No. 4, 1996, pp. 227–236.

[12]Bertin, J. J., *Hypersonic Aerothermodynamics*, AIAA Education Series, AIAA, Washington, DC, 1994, pp. 178–182.

[13]Gentry, A. E., Smyth, D. N., and Oliver, W. R., "The Mark IV Supersonic-Hypersonic Arbitrary Body Program, Volume II," U.S. Air Force Flight Dynamics Lab., AFFDL-TR-73-159, Nov. 1973.

[14]Hecht, A. M., and Nestler, D. E., "A Three-Dimensional Boundary-Layer Computer Program for Sphere-Cone Reentry Vehicles, Volume I—Engineering Analysis and Description," U.S. Air Force Flight Dynamics Lab., AFFDL-TR-78-67, June 1978.

[15]Hankey, W. L., Jr., "Optimization of Lifting Re-Entry Vehicles," Aeronautical Systems Div., ASD-TDR-62-1102, March 1963.

[16]Graham, R. E., and McDowell, J. L., "Simplification of the Wing–Body Interference Problem," *Journal of Aircraft*, Vol. 9, No. 10, 1972, p. 752.

[17]Vukelich, S. R., and Stoy, S. L., "MISSILE DATCOM," U.S. Air Force Wright Aeronautical Labs., AFWAL-TR-86-3091, Wright–Patterson AFB, OH, Dec. 1988.

[18]Bertin, J. J., Martellucci, A., Neumann, R. D., and Stetson, K. F., "Developing a Data Base for the Calibration and Validation of Hypersonic CFD Codes—Sharp Cones," AIAA Paper 93-3044, July 1993.

[19]Ames Research Staff, "Equations, Tables, and Charts for Compressible Flow," NACA Rept. 1135, 1953.

[20]Green, M. J., Lawrence, S. L., Dilley, A. D., Hawkins, R. W., Walker, M. A., and Oberkampf, W. L., "Application of CFD to a Generic Hypersonic Research Study," AIAA Paper 93-0312, Jan. 1993.

[21]Nishio, M., "Visualization of Hypersonic Shock-Wave/Boundary Layer Interaction by Electric Discharge Method," AIAA Paper 97-2288, June 1997.

B. A. Bhutta
Associate Editor